Ultrafast and Local Optoelectronic Transport in Topological Insulators

Jonas Kiemle, Paul Seifert, Alexander W. Holleitner,* and Christoph Kastl*

Recently, topological insulators (TIs) were discovered as a new class of materials representing a subset of topological quantum matter. While a TI possesses a bulk band gap similar to an ordinary insulator, it exhibits gapless states at the surface featuring a spin-helical Dirac dispersion. Due to this unique surface band structure, TIs may find use in (opto)spintronic applications. Herein, optoelectronic methods are discussed to characterize, control, and read-out surface state charge and spin transport of 3D TIs. In particular, time- and spatially-resolved photocurrent microscopy at near-infrared excitation can give fundamental insights into charge carrier dynamics, local electronic properties, and the interplay between bulk and surface currents. Furthermore, possibilities of applying such ultrafast optoelectronic methods to study Berry curvature-related transport phenomena in topological semimetals are discussed.

1. Introduction

Topological materials exhibit band crossings protected by global symmetries and topological invariants.[1–5] For insulators, these band crossing are spatially localized at the crystal surface, and they form chiral edge states as in the quantum (anomalous) Hall phase or helical surface states as in the topological insulator (TI) phase.[1–6] The transition from a trivial insulator to a gapless TI, or equivalently a quantum spin Hall phase, is driven by a spin–orbit interaction, thereby replacing the external magnetic field of the quantum Hall state.[7] The intact time-reversal symmetry of the quantum spin Hall phase dictates that edge (or surface) states which propagate in opposite directions exhibit opposite spin directions.[5] As a consequence, the surface states of TIs have a helical spin texture, where the spin is always locked

J. Kiemle, Prof. A. W. Holleitner, Dr. C. Kastl
Walter Schottky Institute and Physics Department
Technical University of Munich
Am Coulombwall 4a, Garching 85748, Germany
E-mail: holleitner@wsi.tum.de; christoph.kastl@wsi.tum.de

Dr. P. Seifert
ICFO – Institut de Ciencies Fotoniques
The Barcelona Institute of Science and Technology
Castelldefels, Barcelona 08860, Spain

The ORCID identification number(s) for the author(s) of this article can be found under https://doi.org/10.1002/pssb.202000033.

perpendicularly to their momentum.[8] Such helical states represent extraordinary stable quantum states that are robust against smooth changes in material parameters, such as temperature, magnetic field, disorder, or charge density.[5]

The quantum spin Hall phase was experimentally discovered in 2D HgTe/CdTe quantum wells for the first time.[9] There, the bulk bandgap is on the order of millielectronvolt, and electronic transport via the 1D topological edge states becomes only relevant at very low temperatures.[9] In 3D TIs, the 2D surface states have a helical spin texture.[10,11] Importantly, these 3D TIs can exhibit much larger bulk gaps. For example, for the prototypical materials Bi_2Se_3, Bi_2Te_3, and Sb_2Te_3, the bulk energy gaps are on the order of several hundred millielectronvolts. Then, if the Fermi level is adjusted inside the bulk gap, the electronic transport takes place predominantly in the topological surface state, in principle up to room temperature.[12] Nowadays, the topological classification of condensed matter systems has been vastly extended and thousands of materials have been predicted by theory to host topologically protected surface states.[13] The potential applications of TIs span THz detection, plasmonics, (opto)spintronics, and topological quantum information processing.[14–25]

This Review introduces basic concepts of far-field photocurrent spectroscopy on topological materials under a visible to near-infrared optical excitation. For reviews of terahertz optoelectronics and plasmonic effects of TI surface states, we refer to the studies by Politano et al. and Plank and Ganichev.[22,26] To begin with, we discuss the so-called Shockley–Ramo theorem, which establishes the relation between the local photoexcitation and the global photocurrent in gapless surface states. We demonstrate that the scheme allows resolving a quantized photoconductance, when a laser is focused onto the edges of electrostatically gated Hall bars. Then, we elaborate the charge carrier dynamics after an ultrafast optical excitation in Bi_2Se_3.[15] For n-type Bi_2Se_3, the charge carrier dynamics appear on sub-picosecond to picosecond timescales, and they are governed by a heated Fermi–Dirac distribution of conduction electrons. By an on-chip time domain photocurrent spectroscopy, the microscopic mechanisms giving rise to local photocurrents could be experimentally traced, even up to room temperature. The resolved microscopic mechanisms include the photothermoelectric effect and the circular photogalvanic effect. Furthermore, we discuss the impact of reduced bulk doping, exemplarily for Bi_2Te_2Se (BTS) nanowires and nanoplatelets. In BTS, the nonequilibrium charge and spin

populations persist on a timescale of hundreds of picoseconds also at room temperature. Finally, we give a short outlook into the emerging field of topological metals. Herein, we discuss time- and spatially-resolved optoelectronic methods to probe Berry curvature and related transverse transport phenomena in topological metals, such as WTe$_2$.

2. Shockley–Ramo Photocurrents in TIs

In gapless materials, such as TI surface states or Weyl semimetals, the recombination of photoexcited charge carriers happens on a picosecond timescale. Correspondingly, the distance on which excited carriers lose their energy is typically on the order of several hundred nanometers, as inferred for example by time- and angle-resolved photoemission spectroscopy (ARPES),[27–30] optical transient absorption spectroscopy,[31] or ultrafast electro-optical techniques.[32] This stands in stark contrast to, for example, the photoresponse of high-efficiency solar cells. There, photogenerated electrons and holes drift and diffuse over micrometers with lifetimes on the order of microseconds into the charge collecting electrodes. Therefore, the optoelectronic properties of nanoscale conductors are usually governed by the material/contact interface where built-in fields or discontinuities of the electronic properties give rise to charge carrier separation and collection.[33–37] In macroscopic circuits made from gapless materials, photoexcited carriers cannot reach the electrical contacts. Nevertheless, a long-range photocurrent response can be observed in corresponding thin films, including graphene and TIs, where the circuits sizes exceed the effective diffusion length of hot carriers by orders of magnitude.[38–41] In that case, as pointed out first by Shockley and Ramo, long-range effects determine the photoresponse.[42,43] The changing electric field flux of a moving charge induces a current on each electrode. Shockley and Ramo independently proved that, in the electrostatic limit, the global current measured at the electrode is simply given by the local current of the moving charge, projected onto the field distribution between the electrodes with the charge excluded from the system. The latter field is called the weighting field. Later, Pellegrini and others fully generalized the work of Shockley and Ramo to any conducting medium and boundary condition for a generic linear response including retardation effects.[44,45] Recently, Song et al. applied the electrostatic limit of this methodology explicitly to the photocurrent generation in planar, quasi-2D, gapless materials to explain the unconventional photoresponse observed in macroscopic graphene circuits.[38,46] They derived the following expression for the current on the electrode I_{global} induced by a local current density $j_{local}(r)$[46]

$$I_{global} = A \int j_{local}(r) \cdot \nabla \psi(r) d^2r \tag{1}$$

with $\nabla \psi(r)$ being the weighting field between the electrodes, $\psi(r)$ being the corresponding scalar potential, and A accounting for external resistances. The local current density $j_{local}(r)$ can be generated, for example, by a local laser excitation at an arbitrary position within the sample. Importantly, the weighting field, which is a priori almost arbitrary, can be chosen such that it behaves analogously to the physical electric field.[46] Moreover, the global current does not depend on the distance to the electrodes, but rather

on the local geometry and the local photocurrent. In a simple picture, by invoking continuity of current and charge, the local current $j_{local}(r)$ gives rise to an electric field which in turn drives currents into the electrodes far from the excitation region, thereby explaining the long-range character.

Figure 1 shows the photoresponse for a macroscopic Hall bar made from an electronic conductor evaluated within the aforementioned Shockley–Ramo framework. First, the weighting field distribution is calculated for a specific electrode configuration (Figure 1a). Hereby, the source and drain electrodes are at a fixed potential, and all other contacts are floating. Then, the global current is evaluated for each position of the local excitation according to Equation (1). As local excitation, an isotropic Gaussian profile (1 μm width) is assumed, which can arise, for example, from a local laser excitation. We further assume a local photocurrent generation proportional to the gradient of the local excitation profile, which for example holds for a local thermoelectric current with $j_{local}(r) \propto \nabla T(r)$ or a local diffusion current with $j_{local}(r) \propto \nabla n(r)$. For the results shown in Figure 1b, a film with homogeneous electronic properties is assumed. Hence, the photocurrent is completely caused by inhomogeneities of the weighting field, i.e., at the corners of the Hall bars connecting source and drain, as well as at the contacts.[38,46,47] On top, nanoscale inhomogeneities of the film's electronic properties, such as point defects, dielectric disorder, or charge traps[48–50] can introduce significant potential fluctuations, which we model by a random normal distribution (Figure 1c). The resulting photoresponse is dominated by the potential fluctuations in combination with a local photocurrent generation as earlier.[39,40] In turn, it displays a long-range character with the magnitude of the photoresponse being modulated only by the local weighting field and correspondingly by the local geometry (Figure 1d).

2.1. Local Photocurrents and Chemical Potential Fluctuations in TI Thin Films

Photocurrent imaging of TI thin films grown by molecular beam epitaxy (Bi$_2$Se$_3$, BiSbTe$_3$, 10–20 nm)[51,52] revealed a disorder dominated Shockley–Ramo response, as shown in Figure 1d with an amplitude on the order of picoampere for a microwatt excitation power.[39,40] In particular, the long-range nature of the photoresponse was reproduced in millimeter-sized Hall bar circuits, and the impact the weighting field on the photoresponse via the distinct geometrical dependence was confirmed (**Figure 2**). In a subsequent study, it was shown that the photocurrent patterns, and therefore the disorder potential, are independent of the top surface morphology, even after nanomechanical thinning of the TI films.[40] Furthermore, tuning the Fermi level of the BiSbTe$_3$ films electrostatically across the charge neutrality point, clear signatures of the Dirac dispersion were revealed in the photoresponse at cryogenic temperatures. Hence, the photocurrent mainly stems from surface states located at the bottom interface between the substrate and the TI film.[40] As the underlying mechanism of photocurrent generation, a photothermoelectric effect was identified: local potential fluctuations result in a spatially varying Seebeck coefficient $S(r)$, and in turn, the local photocurrent is given as $j_{local}(r) = -\sigma(r)S(r)\nabla T(r)$, where $\nabla T(r)$ is the heat gradient
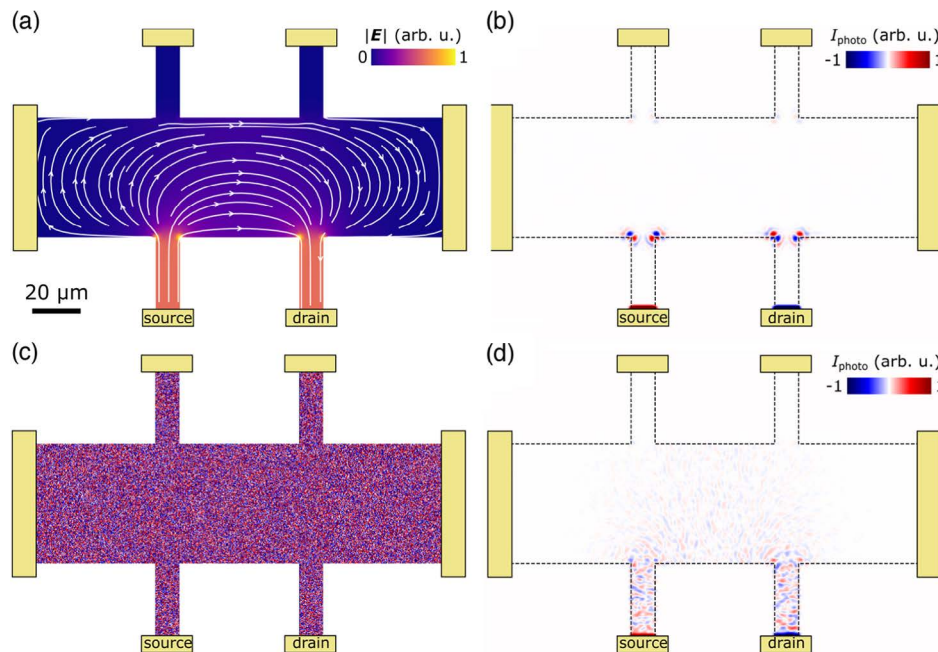
Figure 1. Shockley–Ramo photoresponse of a macroscopic gapless 2D material. a) Electrostatic weighting field of a typical Hall bar circuit calculated by finite element simulation. Source and drain contacts are at a fixed potential, and all other contacts are floating. The color denotes the magnitude of the field and the white lines indicate the direction of the field. Metal electrodes are indicated in yellow. b) Calculated global Shockley–Ramo response for a local isotropic excitation due to a Gaussian laser spot with 1 μm spot size. For an isotropic material, only local inhomogeneities of the weighting field caused by the contacts and the corners result in a photoresponse. c) Assumed random potential fluctuations leading to an inhomogeneous background potential. The color denotes the relative amplitude of the fluctuations. d) Global Shockley–Ramo response for the same local isotropic excitation as in (b) but considering the inhomogeneous background potential from (c). The potential fluctuations dominate the photoresponse.
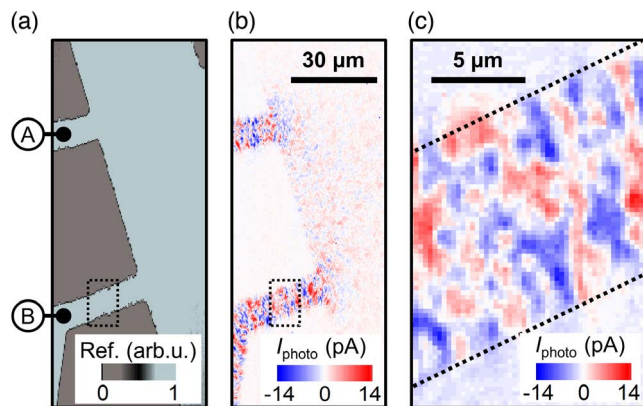

Figure 2. Shockley–Ramo photoresponse in TI thin films with potential fluctuations. a) Reflectance image of a Bi_2Se_3 (blue) film patterned into a Hall bar circuit. The source and drain contacts are labeled A and B. All other contacts are floating. b) Scanning photocurrent map of the circuit revealing a photocurrent pattern, as shown in Figure 1d. c) Photocurrent map of the area marked by dashed rectangle in (a) and (b). The photocurrent patterns are highly reproducible, and their apparent spatial extent is determined by the laser spot size (800 nm). Reproduced with permission.[39] Copyright 2012, American Institute of Physics.

induced by the laser excitation.[40] Based on this model, the magnitude of the potential fluctuations could be estimated to be as large as 10 meV averaged across the lateral extent of the laser spot ($\approx$800 nm).[40] However, the magnitude of the potential

fluctuation at their intrinsic length scale ($\approx$ few nanometers) can be substantially larger, as suggested by theory and scanning tunneling microscopy.[49,53–57] Especially when the Fermi level is close to the Dirac point, such fluctuations can lead to charge puddles[50,58,59] due to the reduced screening in 2D, thereby obscuring the pristine low-energy physics near the Dirac point. Recent advances in fabricating clean van der Waals heterostructures were enabled by the successful reduction of interfacial and dielectric disorder, in particular by the encapsulation of 2D films in hexagonal boron nitride.[41,48,60] Yet, the role of disorder has been studied to a much lesser extent in TIs. The aforementioned experiments provide a simple means to elucidate the impact of potential fluctuations on the transport properties of TIs. Thereby, these findings may have implications for optimizing the growth of thin topological films by molecular beam epitaxy[51,52,61,62] as well as for interpreting magnetotransport in electronically disordered systems.[51,63]

2.2. Quantized Photoconductance

While the aforementioned Shockley–Ramo response is apparent for material anisotropies, such as potential fluctuations or in proximity of metallic contacts,[46] it also allows detecting currents which are more intrinsic in nature. A particularly interesting situation arises for a local excitation at the edge of a 2D system, where rotational and translational symmetries are explicitly broken. Such an optical excitation will drive a net flow of hot charge carriers perpendicular to the edge (**Figure 3**a). Yet, if
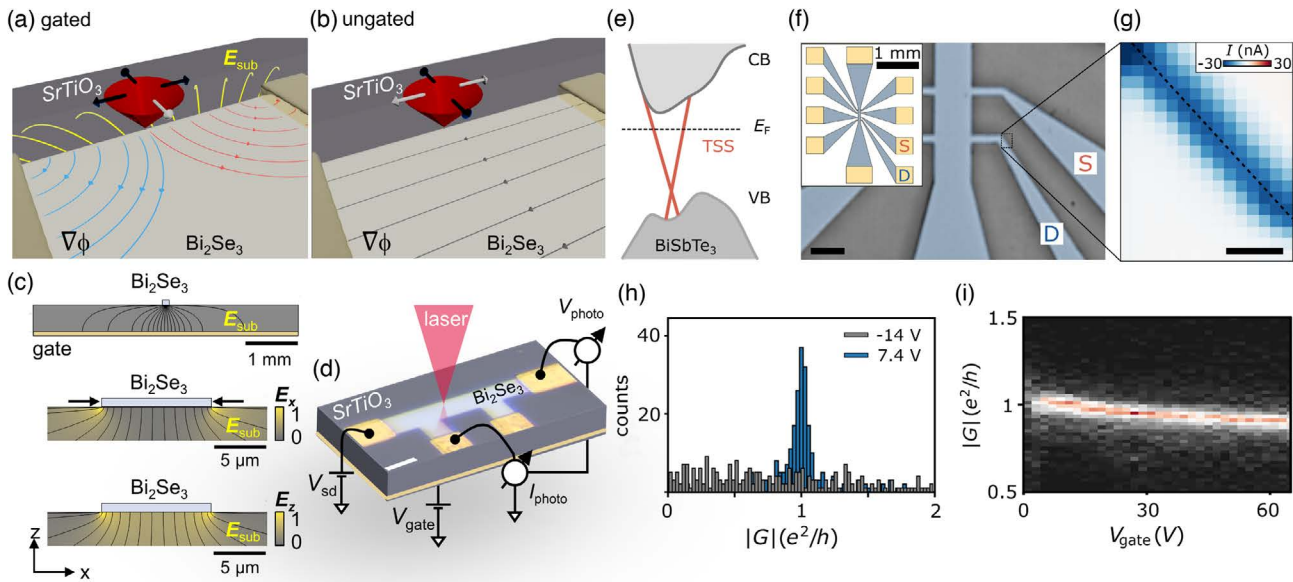
Figure 3. Shockley–Ramo response and quantized conductance in gated circuits. a) Sketch of a thin BiSbTe₃ film on a SrTiO₃ substrate with field lines. The weighting field $\nabla\Phi$ exhibits a component perpendicular to the edge. A local excitation of the surface state (red Dirac cone) at the edges generates a net charge and spin current perpendicular to the edge (gray arrow). This local current couples to the source–drain electrodes (left and right) through the weighting field. b) The weighting field aligns parallel to the circuit edges, and the measured charge and spin (gray arrows) currents parallel to the edge average to zero. c) Electrostatic field distribution between the TI film and the macroscopic bottom gate electrode (at $V_{gate} = 100$ V) calculated by finite element simulation. The fields are in units of 10^7 Vm^{-1}. The large dielectric constant of the SrTiO₃ substrate enhances the in-plane component E_x of the gate field E_{sub} near the edges of the thin film, as indicated by the arrows. d) Bi₂Se₃ circuit with concurrent photocurrent I_{photo} and photovoltage V_{photo} mapping. e) Schematic band structure of bulk insulating BiSbTe₃. f) Macroscopic Hall bar circuit of BiSbTe₃ film. Scale bar, 50 μm. g) Photocurrent map of the area indicated by dashed rectangle in (f). The current is localized at the edge (dashed line). Scale bar, 1 μm. h) Histogram of the local conductance defined as $G = I_{photo}/V_{photo}$. At $V_{gate} = -14$ V, the quantized conductance detection is switched off (gray bars). i) $|G|$ as a function of V_{gate}. Reproduced with permission.[64] Copyright 2019, American Physical Society.

the weighting field is parallel to the sample edge, still all current components to the contacts average out (Figure 3b), and no Shockley–Ramo response can be detected. Only if the weighting field has a non-negligible component perpendicular to the edge, the local current perpendicular to the edge can be detected globally (Figure 3a). Such a photoresponse was demonstrated in planar graphene devices.[47] There, distortions of the in-plane electric field at the corners of microfabricated constrictions create a strong local photoresponse, similar to the situation shown in Figure 1b. A further distortion of the weighting field arises in gated devices, as shown in Figure 3a exemplarily for a Bi₂Se₃ film on a SrTiO₃ substrate.[64] There, the large dielectric constant of the SrTiO₃ substrate ($\varepsilon_r \approx 10^4$ at 4.2 K) results in a strong in-plane component near the edges of the TI film (Figure 3c).[64] The simulated in-plane field can be as high as 10^7 Vm^{-1} for typical experimental parameters ($V_{gate} = 100$ V). Consequently, the boundary conditions for the in-plane weighting field must be adjusted, and a local photocurrent I_{photo} perpendicular to the sample edge can be detected at the contacts for $V_{gate} > 0$ (Figure 3a). In TI circuits (Figure 3d), such a gate-activated Shockley–Ramo response was demonstrated for Bi₂Se₃ and BiSbTe₃ (Figure 3e) up to 10 K for an interband excitation with a photon energy of 1.5 eV. The photoresponse arises at the edges of the circuits (Figure 3f,g).[64] Its amplitude is increased by about two orders of magnitude compared with the fluctuation-induced photoresponse, which were concurrently measured in the samples

but with lower amplitude (Figure 2). Furthermore, it was shown that the photovoltage V_{photo} induced by the local current can be concurrently mapped by a three-terminal measurement. The three-terminal configuration defines a local conductance $G = I_{photo}/V_{photo}$ per laser spot (Figure 3d). Intriguingly, this local conductance is quantized at e^2/h for both Bi₂Se₃ and BiSbTe₃ (Figure 3h), and the detection can be switched on and off by the gate field (Figure 3i). The local conductance quantization occurs irrespective of the circuit's global conductance.[64]

To explain the quantized photoconductance, one needs to consider that the millimeter-sized circuits exceed the relevant transport lengths, such as the mean free path ($\approx$10–100 nm) and the diffusion length of hot charge carriers (several hundred nanometers).[41] Therefore, the quantized conductance has to be understood as a local effect. However, the detection mechanism can be explained by the aforementioned long-range Shockley–Ramo response.[64] The long-range detection stands in stark contrast to the Landauer–Büttiker description of quantized conductance and previous mesoscopic optoelectronic detection schemes, which require a coherent transport between the current and voltage probes.[65–67] The observed conductance of e^2/h suggests spin-polarized transport, which is consistent with the helical dispersion of the topological surface states. For excitation near the sample edge, a net photocurrent is locally generated if the propagation of charge carriers toward the sample edge is effectively cut off, possibly by localized scattering sources.

The Shockley–Ramo readout scheme may be utilized for detecting local quantum transport[45] in further nontrivial gapless systems, such as graphene, Weyl semimetals, or quantum spin Hall insulators. Near-field techniques can further be used to improve the spatial resolution of the photoconductance imaging beyond the diffraction limit of the optical excitation to resolve the interplay of different length scales governing the local photoresponse. The relevant length scales are the Thomas–Fermi screening length (a few nanometers), the inelastic mean free path, the diffusion length of hot carriers, and the optical excitation volume.[40,41]

3. Ultrafast Optoelectronics of TI Surface States

3.1. Charge Carrier Dynamics in TIs

The band structure of TIs and charge carrier dynamics after optical excitation have been well studied both theoretically by density functional theory and experimentally by (time-resolved) ARPES.[15,68–73] **Figure 4**a shows the schematic band structure of the prototypical TI Bi_2Se_3.[11] Nominally, the bulk band structure is gapped by an energy gap of ≈ 0.3 eV between the valence and conduction bands. However, as-grown crystals tend to be n-doped with the Fermi level located in the bulk conduction bands.[51] The bulk bands are interconnected by the topological surface states, which form a Dirac cone with helical spin texture. For a typical optical excitation energy of ≈ 1.5 eV, various transitions from the fully occupied valence band up to the (partially) empty conduction and even into unoccupied topological surface states can be excited (Figure 4a).[15,69,71] Directly after the optical
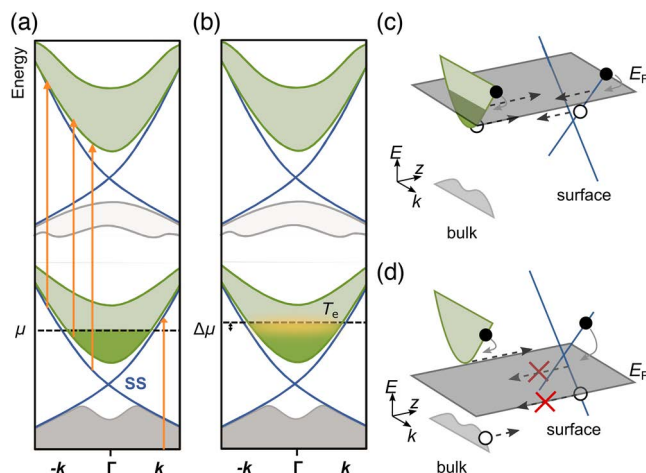

Figure 4. Optical excitation and charge carrier dynamics. a) Schematic of n-type Bi_2Se_3 with partially filled conduction band states, valence band states, topological surface state, and unoccupied higher order bands. Optical excitations at typical experimental photon energies can excite various transitions between surface and bulk bands. b) After initial thermalization on a femtosecond timescale, the dynamics are governed by picosecond cooling of hot carriers near the Fermi edge described by a heated Fermi-Dirac distribution with electron temperature T_e and shifted chemical potential $\mu + \Delta\mu$. c) For bulk conducting TIs, bulk to surface scattering and vice versa are allowed, and the carrier relaxation is described by a common decay time. d) For bulk insulating TIs, the suppressed surface to bulk scattering leads to the formation of a persistent surface state population and a surface photovoltage on a timescale up to the microsecond regime.

transition, the excited electrons and holes form a high energetic nonthermal population in the bulk conduction and valence band as well as in the topological surface states. Polarized illumination can additionally induce a net spin polarization after the excitation via angular momentum selection rules.[74–76] The nonequilibrium population depolarizes and thermalizes via fast carrier–carrier interaction. The resulting ensemble can be described by a heated Fermi–Dirac distribution with electron temperature T_e and shifted chemical potential $\mu + \Delta\mu$ (Figure 4b).[15,70,77] For $T_e > 600$ K, the hot electron distribution relaxes on a sub-picosecond timescale $\tau_{optical} < 1$ ps mediated by optical phonon scattering in the bulk as well as at the surface. For $T_e < 600$ K, bulk relaxation via 3D acoustic phonons dominates on a timescale $\tau_{acoustic} \approx 4$ ps.[70,77] Interestingly, the cooling of surface states is significantly slowed down for $T_e < 600$ K, which is attributed to the weak electron–phonon coupling of the surface state in Bi_2Se_3.[78] In addition, in the topological surface states, the cooling of 2D Dirac fermions via acoustic phonon scattering strongly depends on the charge carrier density.[77] At high doping levels in bulk conducting TIs, charge carrier scattering and diffusion between bulk and surface states are allowed (Figure 4c).[79] Then, bulk and surface state relaxation are comparable, and the carrier relaxation is well described by a common decay time.[79] In bulk insulating TIs, however, the surface state carriers populate in-gap states after the initial thermalization. As a consequence, the carrier scattering from bulk to surface states is generally allowed, but the surface to bulk scattering is forbidden (Figure 4d).[79] Due to the differing mobilities of electrons and holes, bulk to surface scattering leads to the formation of a surface photovoltage and a corresponding metastable surface state population after optical excitation. This surface population cannot decay effectively via phonon scattering or surface to bulk diffusion which results in relaxation times up to several microseconds.[79–81]

3.2. On-Chip Picosecond Time-Domain Photocurrent Spectroscopy

To temporally resolve the ultrafast charge carrier dynamics of TIs in the transport signal, a pump-probe time-domain photocurrent scheme based on stripline circuits can be utilized.[82–85] **Figure 5**a shows a typical sample geometry. A thin Bi_2Se_3 film is contacted by two metal striplines, which act as high-frequency transmission lines.[85,86] The Bi_2Se_3 film is optically excited by a femtosecond optical pump-pulse (with photon energy $E_{photon} \approx 1.5$ eV). The resulting in-plane transient response couples to the field modes of the stripline circuit (Figure 5b), giving rise to a propagating terahertz pulse within the striplines. Finally, a field probe samples the transient electric field via an Auston-photoswitch based on ion-implanted silicon with a photocarrier lifetime $\tau < 1$ ps (Figure 5a).[37] The dispersion and attenuation of the stripline circuit typically limit the bandwidth to ≈ 1–2 THz (Figure 5c).[84,85,87] In turn, the optoelectronic response of the Bi_2Se_3 can be detected via the sampling current $I_{sampling}(\Delta t)$ with a (sub-)picosecond time resolution.

Compared with direct time or frequency domain sampling, using e.g., simply an oscilloscope or a network analyzer, the presented on-chip terahertz spectroscopy provides orders of magnitude improved bandwidth and sensitivity. Furthermore, the
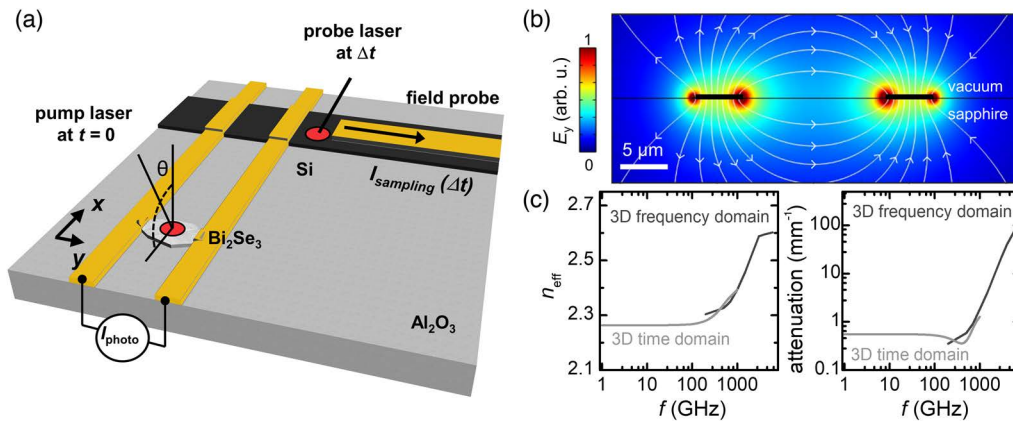
Figure 5. Ultrafast on-chip circuits with TIs. a) A Bi_2Se_3 film on a sapphire substrate is optically excited by a pulsed pump laser (200 fs, 1.5 eV) at an angle of incidence θ. The transient photocurrent couples into the terahertz striplines. At a time-delay Δt, the time-resolved photocurrent $I_{sampling}$ (Δt) is read-out utilizing a silicon-based Auston switch triggered by a probe pulse. The time-integrated photocurrent I_{photo} is measured directly between the contact electrodes. Reproduced under the terms of the Creative Commons CC BY 4.0 license.[86] Copyright 2015, Nature Publishing Group. b) Simulated finite element simulation of an even electric field mode between the striplines. c) Frequency-dependent effective refractive index n_{eff} and attenuation for a coplanar gold stripline on sapphire at room temperature. At frequencies $f > 1$ THz, attenuation and dispersion limit the bandwidth of the detection circuit. Reproduced with permission.[85] Copyright 2017, IEEE.

on-chip pump-probe sampling also obliterates the necessity of matching the impedance of the topological and nanoscale materials under test to the external measurement circuitry.[34,82,83,85] A comparable temporal resolution can be achieved by optoelectronic autocorrelation schemes, which, however, rely on saturating the electronic response by the pump pulse and necessitate large pump fluences.[36,88] Finally, electro-optic sampling of the THz radiation emitted into the far-field after optical pumping can be used to infer information on transient currents and terahertz conductivity inside the material. The latter technique enables extremely high temporal resolution down to a few femtoseconds, only limited by the duration of the probe pulse.[32,89] However, it is limited to fast processes that radiate strongly into the far-field, such as for example shift currents.[32,90] By contrast, the stripline circuits act effectively as near-field antennas probing a multitude of charge transport phenomena, such as thermoelectric currents, drift-diffusion currents, displacement currents, or photo-Dember effects, on various timescales from nanoseconds to sub-picoseconds.[33,36,37,85,91]

3.3. Femtosecond Switching of Surface Currents via Photon Helicity Control

The bulk inversion symmetry of tetradymite chalcogenides precludes the occurrence of a bulk photogalvanic effect by symmetry.[26] At the surface, however, the crystal symmetry is reduced, and a circular photogalvanic effect becomes symmetry-allowed under an oblique angle of incidence (angle θ in Figure 5a).[92] By these symmetry arguments, photogalvanic effects form an effective toolbox to study surface related phenomena in typical TI compounds.[12,93,94] Furthermore, photogalvanic effects can provide a direct measure of Berry curvature in materials with nontrivial band topology.[95,96] General care must be taken to differentiate photogalvanic currents from photon drag currents. The latter show a qualitatively similar polarization

dependence as the photogalvanic currents, but a distinctly different dependence on photon momentum.[97] The selective optical coupling to helical surface states offers the potential for the optical control of spin and charge currents in TIs. In particular, the circular photogalvanic effect can generate terahertz transients at the surface of TIs, which result from a helicity-dependent asymmetric optical excitation of surface states in momentum space.[85,98,99]

Experimentally, the excitation polarization is usually adjusted by a quarter waveplate. The time-integrated photocurrent can be described phenomenologically as (line fit in **Figure 6**a)

$$I_{photo} = C \sin(2\alpha) + L_1 \sin(4\alpha) + L_2 \cos(4\alpha) + D \quad (2)$$

where α is the angle of the quarter wave plate, C is the amplitude of the circular photogalvanic effect, L_1 and L_2 are the amplitudes of the linear photogalvanic effect, and D is the polarization-independent bulk current.[86,92] At the used excitation energy of 1.5 eV, optical transition between surface as well as bulk states are possible (Figure 4). To elucidate the microscopic origin of the photogalvanic effect, several studies investigated the wavelength dependence and Fermi-level dependence either by electrostatic gating or systematic doping of the TI films.[100–103] As the underlying mechanism, asymmetric optical transitions between the topological surface states and bulk bands were identified.[100]

Figure 6b shows the time-resolved photocurrent of a Bi_2Se_3 thin film for varying excitation polarization, which was measured by the aforementioned on-chip spectroscopy (Figure 5a).[86] The photogalvanic current of the topological surface state appears as a quasi-instantaneous response with a lifetime of ≈ 1 ps (red and blue shaded areas in Figure 6b). Importantly, its amplitude and sign are uniquely controlled by the photon polarization (Figure 6c,d) in perfect agreement with the conventional time-integrated measurement (Figure 6a) at the same oblique angle of incidence.[86] At later times (>1 ps), the onset of hot electron currents is resolved with a lifetime of several picosecond consistent with results from time-resolved ARPES.[29,68,70] A more
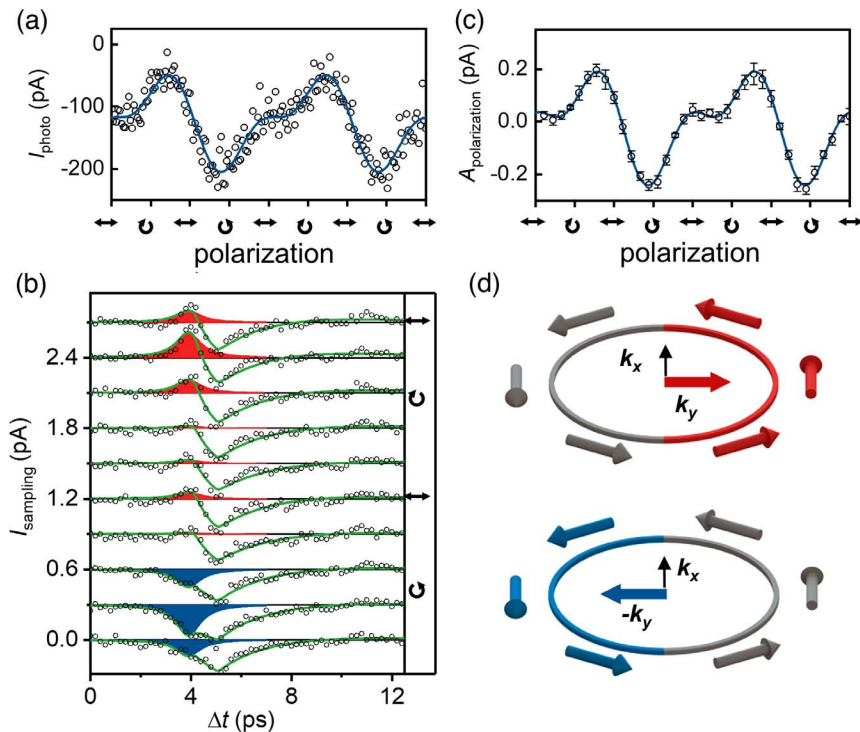
**ADVANCED
SCIENCE NEWS**

www.advancedsciencenews.com

pss b
physica status solidi

www.pss-b.com

Figure 6. Ultrafast circular photogalvanic effect in TIs. a) Time-integrated photocurrent as function of excitation polarization for a Bi_2Se_3 thin film showing a linear and circular photogalvanic effects with a fit according to Equation (2). b) Time-resolved photocurrent $I_{sampling}$ as a function of the time delay and the excitation polarization measured in an ultrafast on-chip circuit, as shown in Figure 5. Red and blue peaks are the polarization-controlled ultrafast currents. c) Polarization-dependent component of $I_{sampling}$ with a fit according to Equation (2) demonstrating an ultrafast circular photogalvanic effect in the Bi_2Se_3. d) Schematic of the photogalvanic current in the direction of k_y to the right contact (red) or $-k_y$ to the left contact (blue) with an in-plane spin polarization. Reproduced under the terms of the Creative Commons CC BY 4.0 license.[86] Copyright 2015, Nature Publishing Group.

detailed analysis of the temporal evolution of the ultrafast photogalvanic currents, which considered the dispersion and attenuation of the stripline circuits, yielded an upper bound of 670 fs for the temporal duration of the photogalvanic current.[85] Thereby, the experimental results suggest that the spin and momentum relaxation govern the dynamics of the photogalvanic surface currents. Time-resolved ARPES experiments indicate that interband transitions at mid-infrared energies below the bulk gap generate substantial photogalvanic surface currents with prolonged lifetimes.[27,104] Ultrafast spin phenomena may be utilized to further extend the fundamental bandwidth limit of TI-based photodetectors, photoswitches, or terahertz sources above the terahertz regime compared with charge-based photoswitches.[105,106] Further ARPES studies demonstrated that the k-space distribution of TI states, and therefore the ultrafast surface currents, can be manipulated not only via optical interband transitions and their corresponding selection rules,[27,107] but also via the coherent interaction between the surface bands and a strong infrared field.[108,109]

3.4. Surface State Photoconductance

For many TIs, the surface lifetime is only a few picoseconds as described in the previous sections. BTS, however, was reported to exhibit surface states with long lifetimes even up to microseconds and relatively short-lived bulk states with a lifetime in the range of several tens of picoseconds.[80,110] A charge drift

caused by a surface photovoltage was attributed to explain the difference. As a compensated TI, BTS has a relatively low residual carrier concentration in the bulk, such that the charge and spin transport is dominated by its topological surface states.[111,112] Finally, BTS can be grown in the form of nanowires, which is advantageous for future information technology circuits with a nanoscale footprint.[113,114]

Figure 7a shows a BTS nanowire integrated into an on-chip terahertz circuit. The circuit is equivalent to the one shown in Figure 5. A pulsed pump laser excites the BTS nanowire, and a time-delayed probe laser reads out the sampling current $I_{sampling}(\Delta t)$ at a distanced metallic field probe (Figure 7b). The surface and bulk states contribute at different timescales to the overall pump laser-induced transient current across the BTS nanowire. Figure 7c shows $I_{sampling}$ for the nanowire. A fast current contribution (red) with a timescale of $\tau_{fast} = 46 \pm 6$ ps was related to the hot carrier dynamics in the bulk states of the nanowire driven by an applied bias voltage V_{sd}.[110] Because of the peculiar setting of the Fermi energy in BTS within the surface states, the second current contribution with $\tau_{second} = 439 \pm 32$ ps (blue) was interpreted to stem from the surface states of the nanowire. Very similar timescales were found for platelets formed from BTS by both terahertz time domain spectroscopy and by time-resolved ARPES measurements,[80,115] such that the surface current dynamics appear to be independent from the nanowire configuration. Figure 7c shows another aspect of
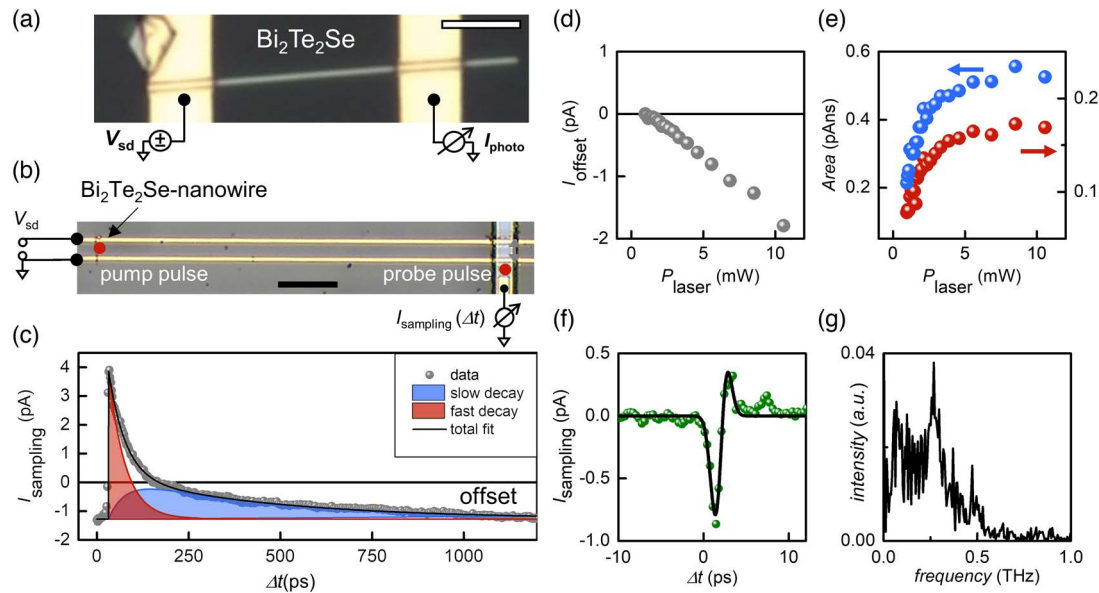
Figure 7. Ultrafast photocurrents and terahertz generation in topological Bi_2Te_3Se-nanowires. a) Optical microscope image of a BTS nanowire. b) The nanowire is integrated into an ultrafast terahertz-time domain photocurrent spectroscopy circuit with bias voltage V_{sd}. Scale bar is 30 μm. c) Time-resolved photoresponse for $V_{sd} = 2\,V$ with a pump pulse focused onto the center of the nanowire ($E_{photon} = 1.54\,eV$, pulse duration ≈150 fs, room temperature). The fast dynamics (red curve) are associated with bulk carriers, the slower dynamics (blue curve) are associated with surface state carriers, and the offset is due to a bolometric photoconductance. d,e) Power dependence of the bolometric and surface (bulk) photoconductance, respectively. f) Time-resolved photoresponse at very short timescales reveals terahertz generation in the nanowire ($V_{sd} = 0\,V$). g) Fast Fourier transformed power spectrum of the terahertz response. Reproduced with permission.[110] Copyright 2017, American Chemical Society (further permissions related to the material excerpted should be directed to the ACS).

BTS. As it is metallic at room temperature, a bolometric photocurrent can give rise to a negative offset current on top of the rather short-lived bulk and surface states' currents. Seifert et al. simulated the quasistationary heat profile of the BTS nanowire excited with a pulsed laser with a repetition frequency of 80 MHz.[110] The corresponding heat diffusion has a timescale of several nanoseconds and can increase the crystal temperature up to 100 K at the laser spot. The bolometric contribution depends linearly on the laser power and has a negative sign as expected for metals (Figure 7d). By contrast, the current contributions from the surface and bulk states have a positive sign, and they saturate for an intensity exceeding 4 mW (Figure 7e).[110] In turn, the pulsed photoconductance of BTS nanowires peculiarly can change sign as a function of laser power. On top, the ultrafast photocurrent spectroscopy revealed that THz radiation is generated occurring in the Schottky depletion field of the metal contacts (Figure 7f,g). The observed bandwidth is significantly lower than the record bandwidth of 40 THz as was achieved by an ultrafast charge transfer along individual bonds in Bi_2Se_3.[32] However, the results of Figure 7 show that BTS nanowires can effectively act as terahertz generators in on-chip circuits at room temperature.

3.5. Spin Hall Photoconductance

After optical excitation, the topological surface states and the bulk states are widely described as a coupled system (Figure 4 and Section 3.4). At the same time, the bulk of 3D TIs supports the generation of a pure transverse spin current j_s in the presence

of an electric field E, which is mediated by the spin Hall effect in the bulk states.[116] In an ideal TI with insulating bulk, the topological connection of the surface bands demands a respective pure spin current through the bulk in the presence of spin relaxation.[116] Such a bulk spin Hall effect was detected in a laser helicity-resolved optoelectronic experiment (**Figure 8**). An exfoliated BTS crystal was contacted via two Ti/Au contacts, and a bias voltage V_{sd} drove a charge current j through the BTS.[115] The bulk spin current j_s is always transverse to the charge current in the metallic surface states and it transports spins between the topological surface states with opposite spin helical structure. Under a circularly polarized excitation near the edges of the platelet, the bulk spin Hall effect drives a spin polarization at the vertical side facts. In turn, the spin polarization can be detected as a helical photoconductance of the surface states (Figure 8a). Figure 8b shows an image of an electrically contacted 90 nm-thick BTS flake. The corresponding laser-helicity-resolved photoconductance maps for opposite current directions (Figure 8c,d) display a helicity-dependent photoconductance with opposite sign at the edges of the BTS flake. These signals reflect the difference $\Delta G_{helical} = G_{helical}(\sigma-) - G_{helical}(\sigma+)$ of the photoconductance G_{photo} (Figure 8e–g). The absence of a helicity-dependent photoconductance signal at normal incidence away from the edges is consistent with the in-plane spin polarization associated with the top/bottom surface of the flake.[86,117] Furthermore, magneto-optic Kerr rotation measurements at the left edge and right edge of the flake demonstrated bias-dependent Kerr angles θ_k. In these measurements, the sign of θ_k was opposite at opposite edges of the BTS and at opposite applied bias (Figure 8h,j). By contrast, θ_k
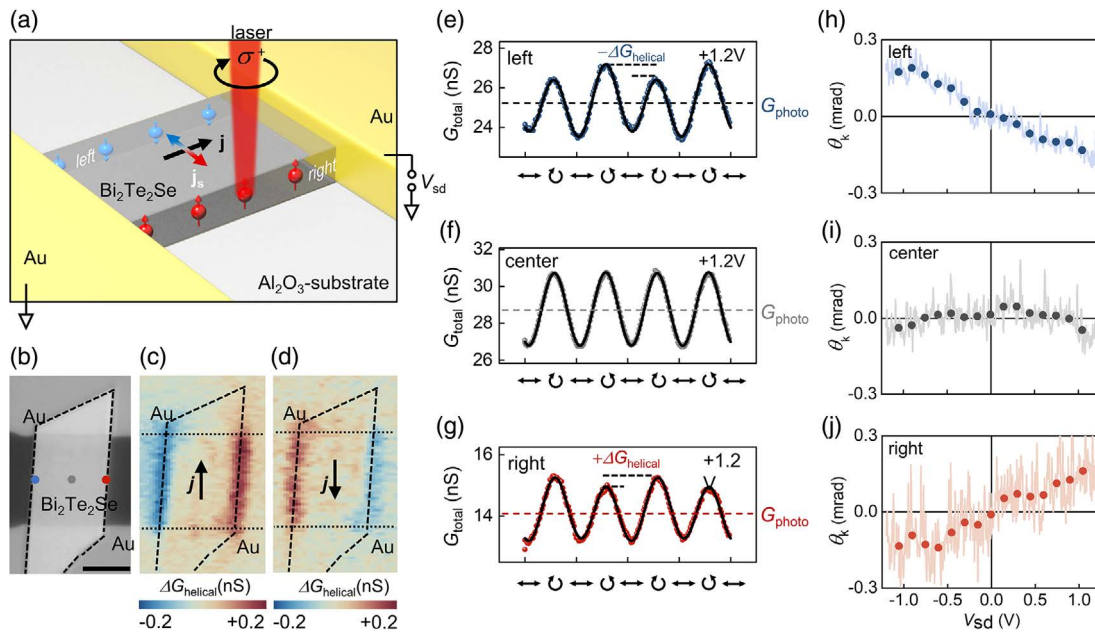
Figure 8. Helicity-dependent edge conductance at room temperature. a) Sketch of a BTS platelet in a metal/TI/metal geometry. Red (blue) spheres represent the electron spin polarization on the right (left) facet of the platelet, when a bias voltage V_{sd} is applied between source and drain. The electron current j gives rise to a transverse spin current j_s. Under circularly polarized excitation at normal incidence near the side facets, optically excited spins are similarly driven into this transverse direction giving rise to a helical photoconductance of the side surface state. b) Optical microscope image of a BTS platelet (highlighted by dashed lines) contacted by two Ti/Au contacts. c,d) Spatial map of the photoconductance generated by the circularly polarized light at $V_{sd} = +1.2$ V (c) and $V_{sd} = -1.2$ V (d). A photoelastic modulator allows detecting the difference $\Delta G_{helical} = G_{helical}(\sigma-) - G_{helical}(\sigma+)$ of photoconductance between $\sigma-$ and $\sigma+$ polarized light. e–g) Total photoconductance G_{total} as a function of the laser polarization at the left edge, right edge, and the center (blue, red, and gray dots in (b)). The symbol $\leftrightarrow$ denotes linearly polarized, $\circlearrowright$ circularly right-polarized light, $\circlearrowleft$ circularly left-polarized light. h–j) Kerr angle θ_k versus V_{sd} at the left edge (h), center (i), and right edge (j) of the BTS platelet. Reproduced under the terms of the Creative Commons CC BY 4.0 license.[115] Copyright 2018, Nature Publishing Group.

vanishes at the center of the platelet (Figure 8i). The bias-dependent Kerr signal was interpreted as a signature of the bulk spin Hall effect-induced spin accumulation. Then, the equal bias dependences of θ_k and $G_{helical}$ indicate that an optical excitation near the side facets can modulate the transverse spin current j_s. The resulting accumulation of spin polarization at the edges enters the measured conductance in the side surface states. In the limit of low disorder, the surface spin relaxation time is identical to the momentum scattering time because of spin momentum locking.[118] In the regime of strong disorder, however, the spin relaxation time can increase for sufficiently small momentum scattering times similar to the regime of motional narrowing in the presence of dominating D'yakonov–Perel spin relaxation.[119–121] Such an enhanced momentum scattering can in fact lead to an increased conductivity at the topological side surfaces in BTS which is modulated under circularly polarized excitation. In the bulk states, the spin Hall effect-mediated spin transport has been shown to be governed by an Elliott–Yafet-type spin relaxation with a spin relaxation time of $\tau_s \approx 5$ ps.[122] The decay time of $G_{helical}$ was found to be $\tau_{decay} = (463 \pm 13)$ ps. While exceeding the spin relaxation time by far, the decay time agrees very well with the surface lifetime of the BTS platelets (Figure 7c for the equivalent material).[110] Hence, $G_{helical}$ prevails as long as τ_{decay} within the surface states of the side facets. Importantly, in an independent study, it was shown that the bulk spin Hall effect-mediated side surface spin conduction exhibits

an exceptionally high charge-to-spin conversion efficiency of up to 35%, which renders such TI nanostructures promising devices for optoelectronic control of spin currents.[122]

4. Beyond TIs: Weyl Semimetals

Recently, the notion of topology in band structure has been greatly expanded beyond TIs.[13] In a simple picture, a material is topological if it exhibits band crossings protected by global symmetries and topological invariants. Initially regarded rare exceptions, recent theoretical studies show that 25% of all materials have such nontrivial bands.[13] For insulators, the bulk is gapped throughout the Brillouin zone. Then, the topological band crossings can only appear at the crystal surface, edges, or corners,[123] where they exhibit a helical dispersion with a single Dirac point. Their stability is ensured by the fact that surface states with opposite helicity are separated in real space on different crystal facets. By contrast, for 3D semimetals, topological band crossings occur in the bulk Brillouin zone.[124] In so-called Weyl semimetals, these band crossings come as pairwise points of opposite chirality and their projection onto the crystal boundaries is accompanied by arc-shaped topological surface states.[125] The stability of the Weyl points is ensured by the separation of these chiral states in momentum space due to an underlying broken inversion symmetry.[125] The resulting Berry curvature $\Omega_n(\mathbf{k})$ of the bands diverges near the topological

Weyl points, which gives rise to a plethora of predicted optoelectronic phenomena, including quantized photogalvanic effect, anomalous Hall effect[20,126] as well as selective coupling between photon and Weyl Fermion chirality.[96,127]

Therefore, the last section of this Review serves as an outlook into the rapidly expanding field of topological materials by exemplarily discussing optoelectronics of the topological semimetal WTe$_2$ and selected Berry curvature-related optoelectronic phenomena.[20,96,126,128–130] The Berry curvature fundamentally impacts the electronic properties of a material via a quantum correction to the band velocity.[131] For an electron with wavevector k and band index n, the band velocity reads

$$v_n(k) = \frac{\partial E_n(k)}{\hbar \partial k} - \frac{e}{\hbar} E \times \Omega_n(k) \tag{3}$$

The second term in Equation (3) is the anomalous velocity from the Berry curvature, which is transverse to the electric field E and results in various Hall effects.[131] Symmetry principles dictate that $\Omega_n(k) = -\Omega_n(-k)$ for a time-reversal invariant system, and $\Omega_n(k) = \Omega_n(-k)$ at the presence of spatial inversion invariance.[131] Then, for a broken time-reversal symmetry, a net Berry curvature can occur when integrating across the Brillouin zone, leading to a net Hall conductivity and a corresponding Hall voltage under applied bias.[131] If inversion symmetry is broken, as for example in the T_d-phase of the Weyl semimetal WTe$_2$ (**Figure 9**a,b), the Berry curvature can exhibit a dipolar structure in the Brillouin zone.[96,131] As a consequence, a nonlinear, crystal-axis-dependent, anomalous Hall effect arises in WTe$_2$, although time-reversal still dictates overall a zero-integrated Berry curvature.[132,133] Alternatively, time-reversal symmetry

can effectively be broken by a circularly polarized optical excitation due to the Berry curvature-dependent chiral selection rules of the Weyl points, which was shown to give rise to a linear photoinduced Hall effect in WTe$_2$.[88] For optoelectronic measurements, the WTe$_2$ crystal was contacted via four electrodes in a multiterminal configuration (Figure 9c). Between two electrodes an external (longitudinal) bias V_{bias} was applied, and along the perpendicular (transversal) direction a photovoltage V_{photo} was measured for a circularly left- and circularly right-polarized excitations, respectively. The exact crystal orientation was determined via polarization-resolved Raman spectroscopy (Figure 9d).[88,134] In such a configuration, a transverse photovoltage can be detected which switches polarity with both the helicity of the exciting laser ($E_{photon} = 1.5$ eV) and with the polarity of the applied external bias (Figure 9e). The corresponding photoinduced transverse (Hall) conductivity is either directly based on the photon chirality[126] or on the corresponding excited spin density in the WTe$_2$.[115,135] Importantly, the linearly bias-dependent transverse photovoltage $V_{helical}$ was found only, if the bias was applied along the a-axis orthogonal to the mirror plane M_a, which is in turn consistent with the anisotropic, dipolar Berry curvature at the Fermi surface.[136] By a time-resolved autocorrelation scheme, the decay time of the photoinduced transversal voltage was found to be on the order of $\tau_{slow} \approx 100$ ps, whereas the decay time of the photoinduced longitudinal current was found to be $\tau_{fast} \approx 2$ ps.[88] An independent study reported a nanosecond spin relaxation time determined by the time-resolved magneto-optical Kerr effect, which was interpreted to be limited by the phonon-assisted recombination of momentum indirect electron–hole pairs.[137] The observed decay time $\tau_{slow} \approx 100$ ps

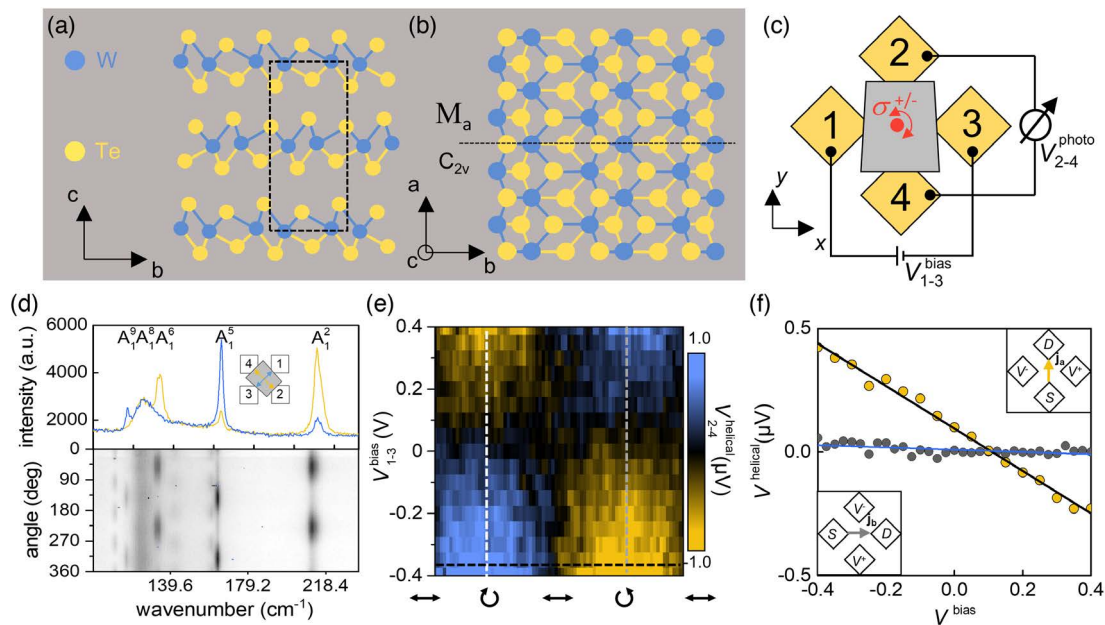**Figure 9.** Polarization-resolved transverse photovoltage spectroscopy of Weyl semimetal WTe$_2$. a) Crystal structure of few-layer WTe$_2$ (side view). In the T_d phase, inversion symmetry is broken along the b-axis. b) Crystal structure of T_d-WTe$_2$ with mirror plane M_a (top view). c) Schematic of the four-terminal photo-Hall voltage geometry. The bias V_{1-3} is applied between the contacts labeled (1) and (3). The transverse voltage V_{2-4} is measured between the contacts labeled (2) and (4). d) Polarization-resolved Raman spectra of WTe$_2$ reveal the crystal orientation. e) Bias dependence of the helicity-dependent contribution to the photovoltage $V_{2-4}^{helical}$. f) Comparison of $V_{helical}$ for V_{bias} applied along the crystal axes orthogonal (yellow, 2–4) and parallel (gray, 1–3) to the mirror plane M_a. Reproduced with permission.[88] Copyright 2019, American Physical Society.

at an excitation pulse length of 150 fs further rules out coherent contributions, such as a light-field-induced anomalous Hall conductivity based on a Floquet state.[126] Therefore, the transverse helical photovoltage was assigned to originate from the long-lived nonequilibrium spin density, which at the microscopic level can drive both a linear spin Hall effect and an anomalous Hall effect. Overall, such optoelectronic spectroscopy can provide a versatile tool to probe Berry curvature-related phenomena and Weyl fermion dynamics in topological metals, which is complementary to conventional transport spectroscopy, such as measurements of the nonlinear Hall effect.[132,133]

5. Conclusion

In conclusion, we report on ultrafast and spatially resolved optoelectronic transport properties of TIs that result from an optical laser pulse excitation in the visible to near-infrared regime. We describe the initial charge and spin carrier relaxation and thermalization processes and show how photothermoelectric currents can give rise to a local photocurrent generation in the surface states. A Shockley–Ramo theorem explains why a photocurrent signal can be detected even on millimeter distances, whereas the intrinsic transport length scales, including the diffusion length of hot carriers and the ballistic transport length, are orders of magnitudes smaller. Applying the same Shockley–Ramo theorem to Hall bars with multiple current and voltage probes further allows resolving a quantized photoconductance in terms of e^2/h in the topological surface states. The dynamical response of the hot carriers in the surface states can be resolved by advanced pump-probe terahertz-time domain photocurrent techniques. Such ultrafast measurements allow distinguishing photogalvanic effects within the surface states from thermoelectric currents and bolometric photoconductance phenomena as well as from terahertz-generation mechanisms within the TIs. Finally, we describe transversal conductance phenomena which can be resolved in optoelectronic measurements. Among these are the spin Hall conductance induced by bias-driven bulk states of TIs and the transversal photovoltage in Berry-phase-dominated topological materials. Especially, the ultrafast measurements demonstrate that TIs can be utilized in optoelectronic high-frequency circuits even at room temperature.

Acknowledgements

Conflict of Interest

The authors declare no conflict of interest.

Keywords

[1] F. D. M. Haldane, *Phys. Rev. Lett.* **1988**, *61*, 2015.
[2] J. E. Avron, L. Sadun, J. Segert, B. Simon, *Phys. Rev. Lett.* **1988**, *61*, 1329.
[3] B. A. Bernevig, S.-C. Zhang, *Phys. Rev. Lett.* **2006**, *96*, 106802.
[4] C. L. Kane, E. J. Mele, *Phys. Rev. Lett.* **2005**, *95*, 226801.
[5] M. Z. Hasan, C. L. Kane, *Rev. Mod. Phys.* **2010**, *82*, 3045.
[6] P. Seifert, C. Kastl, A. Holleitner, in *Encyclopedia of Interfacial Chemistry* (Ed: K. Wandelt), Elsevier, Oxford **2018**, pp. 629–636.
[7] C. L. Kane, E. J. Mele, *Phys. Rev. Lett.* **2005**, *95*, 146802.
[8] A. Rod, T. L. Schmidt, S. Rachel, *Phys. Rev. B* **2015**, *91*, 245112.
[9] M. König, S. Wiedmann, C. Brüne, A. Roth, H. Buhmann, L. W. Molenkamp, X.-L. Qi, S.-C. Zhang, *Science* **2007**, *318*, 766.
[10] D. Hsieh, Y. Xia, D. Qian, L. Wray, J. H. Dil, F. Meier, J. Osterwalder, L. Patthey, J. G. Checkelsky, N. P. Ong, A. V. Fedorov, H. Lin, A. Bansil, D. Grauer, Y. S. Hor, R. J. Cava, M. Z. Hasan, *Nature* **2009**, *460*, 1101.
[11] H. Zhang, C.-X. Liu, X.-L. Qi, X. Dai, Z. Fang, S.-C. Zhang, *Nat. Phys.* **2009**, *5*, 438.
[12] P. Olbrich, L. E. Golub, T. Herrmann, S. N. Danilov, H. Plank, V. V. Bel'kov, G. Mussler, Ch Weyrich, C. M. Schneider, J. Kampmeier, D. Grützmacher, L. Plucinski, M. Eschbach, S. D. Ganichev, *Phys. Rev. Lett.* **2014**, *113*, 096601.
[13] M. G. Vergniory, L. Elcoro, C. Felser, N. Regnault, B. A. Bernevig, Z. Wang, *Nature* **2019**, *566*, 480.
[14] L. Fu, C. L. Kane, *Phys. Rev. Lett.* **2008**, *100*, 096407.
[15] P. Seifert, C. Kastl, A. Holleitner, in *Encyclopedia of Interfacial Chemistry* (Ed: K. Wandelt), Elsevier, Oxford **2018**, pp. 525–534.
[16] P. Schüffelgen, D. Rosenbach, C. Li, T. W. Schmitt, M. Schleenvoigt, A. R. Jalil, S. Schmitt, J. Kölzer, M. Wang, B. Bennemann, U. Parlak, L. Kibkalo, S. Trellenkamp, T. Grap, D. Meertens, M. Luysberg, G. Mussler, E. Berenschot, N. Tas, A. A. Golubov, A. Brinkman, T. Schäpers, D. Grützmacher, *Nat. Nanotechnol.* **2019**, *14*, 825.
[17] J. Han, A. Richardella, S. A. Siddiqui, J. Finley, N. Samarth, L. Liu, *Phys. Rev. Lett.* **2017**, *119*, 077702.
[18] V. Dziom, A. Shuvaev, A. Pimenov, G. V. Astakhov, C. Ames, K. Bendias, J. Böttcher, G. Tkachov, E. M. Hankiewicz, C. Brüne, H. Buhmann, L. W. Molenkamp, *Nat. Commun.* **2017**, *8*, 15197.
[19] L. Wu, M. Salehi, N. Koirala, J. Moon, S. Oh, N. P. Armitage, *Science* **2016**, *354*, 1124.
[20] F. de Juan, A. G. Grushin, T. Morimoto, J. E. Moore, *Nat. Commun.* **2017**, *8*, 15995.
[21] J. Dufouleur, L. Veyrat, B. Dassonneville, C. Nowka, S. Hampel, P. Leksin, B. Eichler, O. G. Schmidt, B. Büchner, R. Giraud, *Nano Lett.* **2016**, *16*, 6733.
[22] A. Politano, L. Viti, M. S. Vitiello, *APL Mater.* **2017**, *5*, 035504.
[23] W. Tang, A. Politano, C. Guo, W. Guo, C. Liu, L. Wang, X. Chen, W. Lu, *Adv. Funct. Mater.* **2018**, *28*, 1801786.
[24] P. D. Pietro, M. Ortolani, O. Limaj, A. D. Gaspare, V. Giliberti, F. Giorgianni, M. Brahlek, N. Bansal, N. Koirala, S. Oh, P. Calvani, S. Lupi, *Nat. Nanotechnol.* **2013**, *8*, 556.
[25] A. Politano, V. M. Silkin, I. A. Nechaev, M. S. Vitiello, L. Viti, Z. S. Aliev, M. B. Babanly, G. Chiarello, P. M. Echenique, E. V. Chulkov, *Phys. Rev. Lett.* **2015**, *115*, 216802.
[26] H. Plank, S. D. Ganichev, *Solid-State Electron.* **2018**, *147*, 44.
[27] K. Kuroda, J. Reimann, K. A. Kokh, O. E. Tereshchenko, A. Kimura, J. Güdde, U. Höfer, *Phys. Rev. B* **2017**, *95*, 081103.

[28] A. Crepaldi, F. Cilento, B. Ressel, C. Cacho, J. C. Johannsen, M. Zacchigna, H. Berger, Ph Bugnon, C. Grazioli, I. C. E. Turcu, E. Springate, K. Kern, M. Grioni, F. Parmigiani, *Phys. Rev. B* **2013**, *88*, 121404.

[29] J. A. Sobota, S.-L. Yang, D. Leuenberger, A. F. Kemper, J. G. Analytis, I. R. Fisher, P. S. Kirchmann, T. P. Devereaux, Z.-X. Shen, *Phys. Rev. Lett.* **2014**, *113*, 157401.

[30] C. Cacho, A. Crepaldi, M. Battiato, J. Braun, F. Cilento, M. Zacchigna, M. C. Richter, O. Heckmann, E. Springate, Y. Liu, S. S. Dhesi, H. Berger, Ph Bugnon, K. Held, M. Grioni, H. Ebert, K. Hricovini, J. Minár, F. Parmigiani, *Phys. Rev. Lett.* **2015**, *114*, 097401.

[31] N. Kumar, B. A. Ruzicka, N. P. Butch, P. Syers, K. Kirshenbaum, J. Paglione, H. Zhao, *Phys. Rev. B* **2011**, *83*, 235306.

[32] L. Braun, G. Mussler, A. Hruban, M. Konczykowski, T. Schumann, M. Wolf, M. Münzenberg, L. Perfetti, T. Kampfrath, *Nat. Commun.* **2016**, *7*, 13259.

[33] A. Brenneis, F. Schade, S. Drieschner, F. Heimbach, H. Karl, J. A. Garrido, A. W. Holleitner, *Sci. Rep.* **2016**, *6*, 35654.

[34] C. Karnetzky, L. Sponfeldner, M. Engl, A. W. Holleitner, *Phys. Rev. B* **2017**, *95*, 161405.

[35] K. Balasubramanian, M. Burghard, K. Kern, M. Scolari, A. Mews, *Nano Lett.* **2005**, *5*, 507.

[36] N. Erhard, A. W. Holleitner, in *Semiconductor Nanowires* (Eds: J. Arbiol, Q. Xiong), Woodhead Publishing, Cambridge **2015**, pp. 365–391.

[37] L. Prechtel, M. Padilla, N. Erhard, H. Karl, G. Abstreiter, A. Fontcuberta, I. Morral, A. W. Holleitner, *Nano Lett.* **2012**, *12*, 2337.

[38] J. Park, Y. H. Ahn, C. Ruiz-Vargas, *Nano Lett.* **2009**, *9*, 1742.

[39] C. Kastl, T. Guan, X. Y. He, K. H. Wu, Y. Q. Li, A. W. Holleitner, *Appl. Phys. Lett.* **2012**, *101*, 251110.

[40] C. Kastl, P. Seifert, X. He, K. Wu, Y. Li, A. W. Holleitner, *2D Mater.* **2015**, *2*, 024012.

[41] A. Woessner, P. Alonso-González, M. B. Lundeberg, Y. Gao, J. E. Barrios-Vargas, G. Navickaite, Q. Ma, D. Janner, K. Watanabe, A. W. Cummings, T. Taniguchi, V. Pruneri, S. Roche, P. Jarillo-Herrero, J. Hone, R. Hillenbrand, F. H. L. Koppens, *Nat. Commun.* **2016**, *7*, 10783.

[42] W. Shockley, *J. Appl. Phys.* **1938**, *9*, 635.

[43] S. Ramo, *Proc. IRE* **1939**, *27*, 584.

[44] B. Pellegrini, *Phys. Rev. B* **1986**, *34*, 5921.

[45] P. D. Yoder, K. Gärtner, W. Fichtner, *J. Appl. Phys.* **1996**, *79*, 1951.

[46] J. C. W. Song, L. S. Levitov, *Phys. Rev. B* **2014**, *90*, 075415.

[47] Q. Ma, C. H. Lui, J. C. W. Song, Y. Lin, J. F. Kong, Y. Cao, T. H. Dinh, N. L. Nair, W. Fang, K. Watanabe, T. Taniguchi, S.-Y. Xu, J. Kong, T. Palacios, N. Gedik, N. M. Gabor, P. Jarillo-Herrero, *Nat. Nanotechnol.* **2019**, *14*, 145.

[48] A. Raja, L. Waldecker, J. Zipfel, Y. Cho, S. Brem, J. D. Ziegler, M. Kulig, T. Taniguchi, K. Watanabe, E. Malic, T. F. Heinz, T. C. Berkelbach, A. Chernikov, *Nat. Nanotechnol.* **2019**, *14*, 832.

[49] H. Beidenkopf, P. Roushan, J. Seo, L. Gorman, I. Drozdov, Y. S. Hor, R. J. Cava, A. Yazdani, *Nat. Phys.* **2011**, *7*, 939.

[50] J. Martin, N. Akerman, G. Ulbricht, T. Lohmann, J. H. Smet, K. von Klitzing, A. Yacoby, *Nat. Phys.* **2008**, *4*, 144.

[51] G. Zhang, H. Qin, J. Chen, X. He, L. Lu, Y. Li, K. Wu, *Adv. Funct. Mater.* **2011**, *21*, 2351.

[52] X. He, T. Guan, X. Wang, B. Feng, P. Cheng, L. Chen, Y. Li, K. Wu, *Appl. Phys. Lett.* **2012**, *101*, 123111.

[53] B. Skinner, T. Chen, B. I. Shklovskii, *Phys. Rev. Lett.* **2012**, *109*, 176801.

[54] Q. Li, E. Rossi, S. Das Sarma, *Phys. Rev. B* **2012**, *86*, 235443.

[55] W. Ko, J. Park, I. Jeon, H. W. Kim, H. Kwon, Y. Oh, J. S. Kim, H. Suh, S. W. Hwang, C. Chung, *Appl. Phys. Lett.* **2016**, *108*, 083109.

[56] J. Dai, D. West, X. Wang, Y. Wang, D. Kwok, S.-W. Cheong, S. B. Zhang, W. Wu, *Phys. Rev. Lett.* **2016**, *117*, 106401.

[57] C. Mann, D. West, I. Miotkowski, Y. P. Chen, S. Zhang, C.-K. Shih, *Nat. Commun.* **2013**, *4*, 2277.

[58] Y. Zhang, V. W. Brar, C. Girit, A. Zettl, M. F. Crommie, *Nat. Phys.* **2009**, *5*, 722.

[59] S. Samaddar, I. Yudhistira, S. Adam, H. Courtois, C. B. Winkelmann, *Phys. Rev. Lett.* **2016**, *116*, 126804.

[60] J. Wierzbowski, J. Klein, F. Sigger, C. Straubinger, M. Kremser, T. Taniguchi, K. Watanabe, U. Wurstbauer, A. W. Holleitner, M. Kaniber, K. Müller, J. J. Finley, *Sci. Rep.* **2017**, *7*, 12383.

[61] J. Kellner, M. Eschbach, J. Kampmeier, M. Lanius, E. Młyńczak, G. Mussler, B. Holländer, L. Plucinski, M. Liebmann, D. Grützmacher, C. M. Schneider, M. Morgenstern, *Appl. Phys. Lett.* **2015**, *107*, 251603.

[62] M. Eschbach, E. Młyńczak, J. Kellner, J. Kampmeier, M. Lanius, E. Neumann, C. Weyrich, M. Gehlmann, P. Gospodarič, S. Döring, G. Mussler, N. Demarina, M. Luysberg, G. Bihlmayer, T. Schäpers, L. Plucinski, S. Blügel, M. Morgenstern, C. M. Schneider, D. Grützmacher, *Nat. Commun.* **2015**, *6*, 8816.

[63] J. Ping, I. Yudhistira, N. Ramakrishnan, S. Cho, S. Adam, M. S. Fuhrer, *Phys. Rev. Lett.* **2014**, *113*, 047206.

[64] P. Seifert, M. Kundinger, G. Shi, X. He, K. Wu, Y. Li, A. W. Holleitner, C. Kastl, *Phys. Rev. Lett.* **2019**, *122*, 146804.

[65] C. Kastl, M. Stallhofer, D. Schuh, W. Wegscheider, A. W. Holleitner, *New J. Phys.* **2015**, *17*, 023007.

[66] M. Stallhofer, C. Kastl, M. Brändlein, C. Karnetzky, D. Schuh, W. Wegscheider, A. W. Holleitner, *Phys. Rev. B* **2012**, *86*, 115313.

[67] K.-D. Hof, F. J. Kaiser, M. Stallhofer, D. Schuh, W. Wegscheider, P. Hänggi, S. Kohler, J. P. Kotthaus, A. W. Holleitner, *Nano Lett.* **2010**, *10*, 3836.

[68] J. Reimann, J. Güdde, K. Kuroda, E. V. Chulkov, U. Höfer, *Phys. Rev. B* **2014**, *90*, 081106.

[69] D. Niesner, T. Fauster, S. V. Eremeev, T. V. Menshchikova, Y. M Koroteev, A. P. Protogenov, E. V. Chulkov, O. E. Tereshchenko, K. A. Kokh, O. Alekperov, A. Nadjafov, N. Mamedov, *Phys. Rev. B* **2012**, *86*, 205403.

[70] A. Crepaldi, B. Ressel, F. Cilento, M. Zacchigna, C. Grazioli, H. Berger, Ph Bugnon, K. Kern, M. Grioni, F. Parmigiani, *Phys. Rev. B* **2012**, *86*, 205133.

[71] J. A. Sobota, S.-L. Yang, A. F. Kemper, J. J. Lee, F. T. Schmitt, W. Li, R. G. Moore, J. G. Analytis, I. R. Fisher, P. S. Kirchmann, T. P. Devereaux, Z.-X. Shen, *Phys. Rev. Lett.* **2013**, *111*, 136802.

[72] M. Hajlaoui, E. Papalazarou, J. Mauchain, G. Lantz, N. Moisan, D. Boschetto, Z. Jiang, I. Miotkowski, Y. P. Chen, A. Taleb-Ibrahimi, L. Perfetti, M. Marsi, *Nano Lett.* **2012**, *12*, 3532.

[73] K. Sumida, M. Kakoki, J. Reimann, M. Nurmamat, S. Goto, Y. Takeda, Y. Saitoh, K. A. Kokh, O. E. Tereshchenko, J. Güdde, U. Höfer, A. Kimura, *New J. Phys.* **2019**, *21*, 093006.

[74] D. Hsieh, F. Mahmood, J. W. McIver, D. R. Gardner, Y. S. Lee, N. Gedik, *Phys. Rev. Lett.* **2011**, *107*, 077401.

[75] J. Sánchez-Barriga, M. Battiato, M. Krivenkov, E. Golias, A. Varykhalov, A. Romualdi, L. V. Yashina, J. Minár, O. Kornilov, H. Ebert, K. Held, J. Braun, *Phys. Rev. B* **2017**, *95*, 125405.

[76] M. C. Wang, S. Qiao, Z. Jiang, S. N. Luo, J. Qi, *Phys. Rev. Lett.* **2016**, *116*, 036601.

[77] J. A. Sobota, S. Yang, J. G. Analytis, Y. L. Chen, I. R. Fisher, P. S. Kirchmann, Z.-X. Shen, *Phys. Rev. Lett.* **2012**, *108*, 117403.

[78] Z.-H. Pan, A. V. Fedorov, D. Gardner, Y. S. Lee, S. Chu, T. Valla, *Phys. Rev. Lett.* **2012**, *108*, 187001.

[79] J. Sánchez-Barriga, M. Battiato, E. Golias, A. Varykhalov, L. V. Yashina, O. Kornilov, O. Rader, *Appl. Phys. Lett.* **2017**, *110*, 141605.

[80] M. Neupane, S.-Y. Xu, Y. Ishida, S. Jia, B. M. Fregoso, C. Liu, I. Belopolski, G. Bian, N. Alidoust, T. Durakiewicz, V. Galitski, S. Shin, R. J. Cava, M. Z. Hasan, *Phys. Rev. Lett.* **2015**, *115*, 116801.

[81] K. Sumida, Y. Ishida, S. Zhu, M. Ye, A. Pertsova, C. Triola, K. A. Kokh, O. E. Tereshchenko, A. V. Balatsky, S. Shin, A. Kimura, *Sci. Rep.* **2017**, *7*, 14080.

[82] L. Prechtel, L. Song, D. Schuh, P. Ajayan, W. Wegscheider, A. W. Holleitner, *Nat. Commun.* **2012**, *3*, 646.

[83] A. Brenneis, L. Gaudreau, M. Seifert, H. Karl, M. S. Brandt, H. Huebl, J. A. Garrido, F. H. L. Koppens, A. W. Holleitner, *Nat. Nanotechnol.* **2015**, *10*, 135.

[84] C. Karnetzky, P. Zimmermann, C. Trummer, C. D. Sierra, M. Wörle, R. Kienberger, A. W. Holleitner, *Nat. Commun.* **2018**, *9*, 2471.

[85] C. Kastl, C. Karnetzky, A. Brenneis, F. Langrieger, A. W. Holleitner, *IEEE J. Sel. Top. Quantum Electron.* **2017**, *23*, 8700305.

[86] C. Kastl, C. Karnetzky, H. Karl, A. W. Holleitner, *Nat. Commun.* **2015**, *6*, 6617.

[87] N. Fernandez, P. Zimmermann, P. Zechmann, M. Wörle, R. Kienberger, A. W. Holleitner, in *Proc. of Ultrafast Phenomena and Nanophotonics XXIII*, International Society For Optics And Photonics (SPIE), San Francisco **2019**, p. 109160R.

[88] P. Seifert, F. Sigger, J. Kiemle, K. Watanabe, T. Taniguchi, C. Kastl, U. Wurstbauer, A. W. Holleitner, *Phys. Rev. B* **2019**, *99*, 161403.

[89] R. Valdés Aguilar, J. Qi, M. Brahlek, N. Bansal, A. Azad, J. Bowlan, S. Oh, A. J. Taylor, R. P. Prasankumar, D. A. Yarotski, *Appl. Phys. Lett.* **2015**, *106*, 011901.

[90] K. W. Kim, T. Morimoto, N. Nagaosa, *Phys. Rev. B* **2017**, *95*, 035134.

[91] N. Erhard, P. Seifert, L. Prechtel, S. Hertenberger, H. Karl, G. Abstreiter, G. Koblmüller, A. W. Holleitner, *Ann. Phys. (Berlin)* **2013**, *525*, 180.

[92] J. W. McIver, D. Hsieh, H. Steinberg, P. Jarillo-Herrero, N. Gedik, *Nat. Nanotechnol.* **2012**, *7*, 96.

[93] H. Plank, S. N. Danilov, V. V. Bel'kov, V. A. Shalygin, J. Kampmeier, M. Lanius, G. Mussler, D. Grützmacher, S. D. Ganichev, *J. Appl. Phys.* **2016**, *120*, 165301.

[94] H. Plank, J. Pernul, S. Gebert, S. N. Danilov, J. König-Otto, S. Winnerl, M. Lanius, J. Kampmeier, G. Mussler, I. Aguilera, D. Grützmacher, S. D. Ganichev, *Phys. Rev. Mater.* **2018**, *2*, 024202.

[95] S.-Y. Xu, Q. Ma, H. Shen, V. Fatemi, S. Wu, T.-R. Chang, G. Chang, A. M. M. Valdivia, C.-K. Chan, Q. D. Gibson, J. Zhou, Z. Liu, K. Watanabe, T. Taniguchi, H. Lin, R. J. Cava, L. Fu, N. Gedik, P. Jarillo-Herrero, *Nat. Phys.* **2018**, *14*, 900.

[96] Q. Ma, S.-Y. Xu, C.-K. Chan, C.-L. Zhang, G. Chang, Y. Lin, W. Xie, T. Palacios, H. Lin, S. Jia, P. A. Lee, P. Jarillo-Herrero, N. Gedik, *Nat. Phys.* **2017**, *13*, 842.

[97] H. Plank, L. E. Golub, S. Bauer, V. V. Bel'kov, T. Herrmann, P. Olbrich, M. Eschbach, L. Plucinski, C. M. Schneider, J. Kampmeier, M. Lanius, G. Mussler, D. Grützmacher, S. D. Ganichev, *Phys. Rev. B* **2016**, *93*, 125434.

[98] A. Junck, G. Refael, F. von Oppen, *Phys. Rev. B* **2013**, *88*, 075144.

[99] P. Hosur, *Phys. Rev. B* **2011**, *83*, 035309.

[100] Y. Pan, Q.-Z. Wang, A. L. Yeats, T. Pillsbury, T. C. Flanagan, A. Richardella, H. Zhang, D. D. Awschalom, C.-X. Liu, N. Samarth, *Nat. Commun.* **2017**, *8*, 1037.

[101] K. N. Okada, N. Ogawa, R. Yoshimi, A. Tsukazaki, K. S. Takahashi, M. Kawasaki, Y. Tokura, *Phys. Rev. B* **2016**, *93*, 081403.

[102] J. Duan, N. Tang, X. He, Y. Yan, S. Zhang, X. Qin, X. Wang, X. Yang, F. Xu, Y. Chen, W. Ge, B. Shen, *Sci. Rep.* **2015**, *4*, 4889.

[103] D.-X. Qu, X. Che, X. Kou, L. Pan, J. Crowhurst, M. R. Armstrong, J. Dubois, K. L. Wang, G. F. Chapline, *Phys. Rev. B* **2018**, *97*, 045308.

[104] K. Kuroda, J. Reimann, J. Güdde, U. Höfer, *Phys. Rev. Lett.* **2016**, *116*, 076801.

[105] M. B. Ketchen, D. Grischkowsky, T. C. Chen, C. Chi, I. N. Duling, N. J. Halas, J. Halbout, J. A. Kash, G. P. Li, *Appl. Phys. Lett.* **1986**, *48*, 751.

[106] T. Seifert, S. Jaiswal, U. Martens, J. Hannegan, L. Braun, P. Maldonado, F. Freimuth, A. Kronenberg, J. Henrizi, I. Radu, E. Beaurepaire, Y. Mokrousov, P. M. Oppeneer, M. Jourdan, G. Jakob, D. Turchinovich, L. M. Hayden, M. Wolf, M. Münzenberg, M. Kläui, T. Kampfrath, *Nat. Photonics* **2016**, *10*, 483.

[107] H. Soifer, A. Gauthier, A. F. Kemper, C. R. Rotundu, S.-L. Yang, H. Xiong, D. Lu, M. Hashimoto, P. S. Kirchmann, J. A. Sobota, Z.-X. Shen, *Phys. Rev. Lett.* **2019**, *122*, 167401.

[108] J. Reimann, S. Schlauderer, C. P. Schmid, F. Langer, S. Baierl, K. A. Kokh, O. E. Tereshchenko, A. Kimura, C. Lange, J. Güdde, U. Höfer, R. Huber, *Nature* **2018**, *562*, 396.

[109] F. Mahmood, C.-K. Chan, Z. Alpichshev, D. Gardner, Y. Lee, P. A. Lee, N. Gedik, *Nat. Phys.* **2016**, *12*, 306.

[110] P. Seifert, K. Vaklinova, K. Kern, M. Burghard, A. W. Holleitner, *Nano Lett.* **2017**, *17*, 973. https://pubs.acs.org/doi/full/10.1021/acs.nanolett.6b04312.

[111] Z. Ren, A. A. Taskin, S. Sasaki, K. Segawa, Y. Ando, *Phys. Rev. B* **2010**, *82*, 241306.

[112] J. Tian, I. Miotkowski, S. Hong, Y. P. Chen, *Sci. Rep.* **2015**, *5*, 14293.

[113] H. Peng, K. Lai, D. Kong, S. Meister, Y. Chen, X.-L. Qi, S.-C. Zhang, Z.-X. Shen, Y. Cui, *Nat. Mater.* **2010**, *9*, 225.

[114] D. Kong, J. C. Randel, H. Peng, J. J. Cha, S. Meister, K. Lai, Y. Chen, Z.-X. Shen, H. C. Manoharan, Y. Cui, *Nano Lett.* **2010**, *10*, 329.

[115] P. Seifert, K. Vaklinova, S. Ganichev, K. Kern, M. Burghard, A. W. Holleitner, *Nat. Commun.* **2018**, *9*, 331.

[116] X. Peng, Y. Yang, R. R. P. Singh, S. Y. Savrasov, D. Yu, *Nat. Commun.* **2016**, *7*, 10878.

[117] J. Sánchez-Barriga, E. Golias, A. Varykhalov, J. Braun, L. V. Yashina, R. Schumann, J. Minár, H. Ebert, O. Kornilov, O. Rader, *Phys. Rev. B* **2016**, *93*, 155426.

[118] X. Liu, J. Sinova, *Phys. Rev. Lett.* **2013**, *111*, 166801.

[119] Z. Qiu, J. Li, D. Hou, E. Arenholz, A. T. N'Diaye, A. Tan, K. Uchida, K. Sato, S. Okamoto, Y. Tserkovnyak, Z. Q. Qiu, E. Saitoh, *Nat. Commun.* **2016**, *7*, 12670.

[120] M. I. D'yakonov, *Sov. Phys. Semicond.* **1986**, *20*, 110.

[121] K. Banerjee, J. Son, P. Deorani, P. Ren, L. Wang, H. Yang, *Phys. Rev. B* **2014**, *90*, 235427.

[122] J. Lee, S. Sim, S. Park, C. In, S. Cho, S. Lee, S. Cha, S. Lee, H. Kim, J. Kim, W. Shim, J. S. Kim, D. Kim, H. Choi, *ACS Photonics* **2018**, *5*, 3347.

[123] F. Schindler, A. M. Cook, M. G. Vergniory, Z. Wang, S. S. P. Parkin, B. A. Bernevig, T. Neupert, *Sci. Adv.* **2018**, *4*, eaat0346.

[124] C. Fang, H. Weng, X. Dai, Z. Fang, *Chin. Phys. B* **2016**, *25*, 117106.

[125] A. A. Soluyanov, D. Gresch, Z. Wang, Q. Wu, M. Troyer, X. Dai, B. A. Bernevig, *Nature* **2015**, *527*, 495.

[126] C.-K. Chan, P. A. Lee, K. S. Burch, J. H. Han, Y. Ran, *Phys. Rev. Lett.* **2016**, *116*, 026805.

[127] L. Wu, S. Patankar, T. Morimoto, N. L. Nair, E. Thewalt, A. Little, J. G. Analytis, J. E. Moore, J. Orenstein, *Nat. Phys.* **2017**, *13*, 350.

[128] M. Caputo, L. Khalil, E. Papalazarou, N. Nilforoushan, L. Perfetti, A. Taleb-Ibrahimi, Q. D. Gibson, R. J. Cava, M. Marsi, *Phys. Rev. B* **2018**, *97*, 115115.

[129] E. J. König, H.-Y. Xie, D. A. Pesin, A. Levchenko, *Phys. Rev. B* **2017**, *96*, 075123.

[130] B. Yan, C. Felser, *Annu. Rev. Condens. Matter Phys.* **2017**, *8*, 337.

[131] D. Xiao, M.-C. Chang, Q. Niu, *Rev. Mod. Phys.* **2010**, *82*, 1959.

[132] Q. Ma, S.-Y. Xu, H. Shen, D. MacNeill, V. Fatemi, T.-R. Chang, A. M. M. Valdivia, S. Wu, Z. Du, C.-H. Hsu, S. Fang, Q. D. Gibson, K. Watanabe, T. Taniguchi, R. J. Cava, E. Kaxiras, H.-Z. Lu, H. Lin, L. Fu, N. Gedik, P. Jarillo-Herrero, *Nature* **2019**, *565*, 337.

[133] K. Kang, T. Li, E. Sohn, J. Shan, K. F. Mak, *Nat. Mater.* **2019**, *18*, 324.

[134] Q. Song, H. Wang, X. Xu, X. Pan, Y. Wang, F. Song, X. Wan, L. Dai, *RSC Adv.* **2016**, *6*, 103830.

[135] Y. Liu, J. Besbas, Y. Wang, P. He, M. Chen, D. Zhu, Y. Wu, J. M. Lee, L. Wang, J. Moon, N. Koirala, S. Oh, H. Yang, *Nat. Commun.* **2018**, *9*, 1.

[136] Y. Zhang, Y. Sun, B. Yan, *Phys. Rev. B* **2018**, *97*, 041101.

[137] Q. Wang, J. Li, J. Besbas, C.-H. Hsu, K. Cai, L. Yang, S. Cheng, Y. Wu, W. Zhang, K. Wang, T.-R. Chang, H. Lin, H. Chang, H. Yang, *Adv. Sci.* **2018**, *5*, 1700912.